Monthly Notices
of the
ROYAL ASTRONOMICAL SOCIETY

MNRAS **459,** 2118–2129 (2016)
Advance Access publication 2016 April 5

doi:10.1093/mnras/stw763

# Fast and accurate mock catalogue generation for low-mass galaxies

Jun Koda,[1,2,3]★ Chris Blake,[2] Florian Beutler,[4] Eyal Kazin[2,3] and Felipe Marin[2,3]

[1]*INAF – Osservatorio Astronomico di Brera, via E. Bianchi 46, I-23807 Merate, Italy*
[2]*Centre for Astrophysics and Supercomputing, Swinburne University of Technology, PO Box 218, Hawthorn, VIC 3122, Australia*
[3]*ARC Centre of Excellence for All-sky Astrophysics (CAASTRO)*
[4]*Lawrence Berkeley National Lab, 1 Cyclotron Rd, Berkeley, CA 94720, USA*

Accepted 2016 March 31. Received 2016 March 29; in original form 2015 July 20

## ABSTRACT

We present an accurate and fast framework for generating mock catalogues including low-mass haloes, based on an implementation of the COmoving Lagrangian Acceleration (COLA) technique. Multiple realisations of mock catalogues are crucial for analyses of large-scale structure, but conventional *N*-body simulations are too computationally expensive for the production of thousands of realizations. We show that COLA simulations can produce accurate mock catalogues with a moderate computation resource for low- to intermediate-mass galaxies in $10^{12}\,\mathrm{M}_{\odot}$ haloes, both in real and redshift space. COLA simulations have accurate peculiar velocities, without systematic errors in the velocity power spectra for $k \leq 0.15\,h\,\mathrm{Mpc}^{-1}$, and with only 3-per cent error for $k \leq 0.2\,h\,\mathrm{Mpc}^{-1}$. We use COLA with 10 time steps and a Halo Occupation Distribution to produce 600 mock galaxy catalogues of the WiggleZ Dark Energy Survey. Our parallelized code for efficient generation of accurate halo catalogues is publicly available at github.com/junkoda/cola_halo.

**Key words:** methods: numerical – cosmology: theory – large-scale structure of Universe.

## 1 INTRODUCTION

Generating multiple realisations of mock galaxy catalogues is essential for analysing large-scale structure in the Universe. It is a necessary tool for evaluating the statistical uncertainties in the clustering measurements, and systematic errors in theoretical modelling and data analysis. The importance of accurate mock catalogues is increasing as data analyses become more complicated and sophisticated, and the large-scale-structure measurements become more precise.

One of the targets of cosmological surveys is the Baryon Acoustic Oscillation (BAO) feature imprinted in the galaxy clustering (Cole et al. 2005; Eisenstein et al. 2005; Blake et al. 2011; Beutler et al. 2012; Anderson et al. 2014). It is a 'standard ruler' that provides robust measurements of the expansion history of the Universe through the cosmological distances as a function of redshift. The data analysis procedure was recently refined by the 'reconstruction' technique (Eisenstein et al. 2007), which improves the precision by sharpening the BAO peak by rewinding the large-scale displacements in part. This technique was first applied to the Sloan Digital Sky Survey Data Release 7 (Mehta et al. 2012; Padmanabhan et al. 2012), and has become a standard procedure (Anderson et al. 2012, 2014; Kazin et al. 2014).

Covariance matrices, e.g. $C_{ij} = \langle\xi(r_i)\xi(r_j)\rangle - \langle\xi(r_i)\rangle\,\langle\xi(r_j)\rangle$, for the two-point correlation function $\xi(r)$, need to be calculated for any analyses of large-scale structure to evaluate the best-fitting cosmological parameters and their confidence regions. The ensemble averages for the covariance matrix can be computed directly from many realisations of mock galaxies. The benefit of multiple realisations of mock galaxy catalogues to build the covariance matrix is not limited to BAO, but the preference of using mocks over other methods is clear for BAO due to its large length-scale of 150 Mpc and non-trivial numerical process used by the reconstruction technique. Mock galaxy catalogues based on simulations can properly evaluate the error caused by imperfect reconstruction due to non-linear motions and realistic selection function. Alternative methods like jack-knife sampling work for measurements on small scales, but we often do not have enough quasi-independent subvolumes assumed for jack-knife sampling on BAO scales. Lognormal realizations of the galaxy density field (Coles & Jones 1991) can provide many samples of large-scale fields, but non-linear dynamics is not accurate; one of the sources of uncertainties we would like to evaluate for the BAO measurement is the amount of non-linear motion that is not completely captured by the rewinding in the reconstruction algorithm.

Running many *N*-body simulations for multiple realisations is ideal, but it requires a large amount of computation time on a massively parallel supercomputer. An insufficient number of mock catalogues would give biased error evaluation; even with 600 mocks, careful treatment is necessary to evaluate the inverse covariance matrix (Hartlap, Simon & Schneider 2007; Percival et al. 2014). Simulations will be harder as the survey volume becomes larger (BigBOSS Schlegel et al. 2009), and the resolution required to resolve galaxy-hosting haloes becomes higher, e.g. for emission-line galaxies in the HETDEX (Hill et al. 2004), Euclid (Amendola

★E-mail: jun.koda@brera.inaf.it

et al. 2013), or FastSound (Tonegawa et al. 2015) surveys, or for less-luminous galaxies in deeper surveys, GAMA (Driver et al. 2011) or VIPERS (Garilli et al. 2014). Manera et al. (2013) generated 600 mock galaxy catalogues, 'PThalos', for the Baryon Oscillation Spectroscopic Survey (BOSS), using the second-order perturbation theory and Friends-of-Friends (FoF) halo finder (Davis et al. 1985). Theoretical ideas of fast simulations using analytical theories existed a decade ago (Monaco, Theuns & Taffoni 2002; Scoccimarro & Sheth 2002), or even earlier (adhesion approximation, Gurbatov, Saichev & Shandarin 1989), but such research attracted attention after the practical application to BOSS (de la Torre & Peacock 2013; Monaco et al. 2013; Angulo et al. 2014; Kitaura, Yepes & Prada 2014; White, Tinker & McBride 2014; Avila et al. 2015; Chuang et al. 2015a). See Chuang et al. (2015b) for a comparison of these methods. Some of these recent methods randomly generate haloes, instead of resolving haloes, using a probability that depends on the local dark matter density.

We generate 600 mock galaxy catalogues for the WiggleZ Dark Energy Survey (Drinkwater et al. 2010) for the improved BAO measurement using the reconstruction technique (Kazin et al. 2014) and for other analyses (Burrage, Parkinson & Seery 2015; Beutler et al. 2016; Marín et al. 2016). The WiggleZ samples are emission-line galaxies in dark matter haloes of masses approximately $10^{12}\,\mathrm{M}_{\odot}$, which is about an order of magnitude smaller than the haloes hosting the BOSS constant mass (CMASS) galaxies. We use the COmoving Lagrangian Acceleration (COLA; Tassev, Zaldarriaga & Eisenstein 2013) method to run many simulation realizations, after finding that the PTHalo method by Manera et al. (2013) was not able to resolve $10^{12}\,\mathrm{M}_{\odot}$ haloes (see Section 3.1). In this paper, we present the accuracy of COLA mocks on large scales relevant to cosmological analyses, which was not tested with the small simulation box by Tassev et al. (2013), and show that COLA is accurate not only for massive CMASS-like galaxies (Chuang et al. 2015b) but for lower-mass galaxies. COLA is becoming a common tool when a large number of simulations is required (Howlett, Manera & Percival 2015a; Howlett et al. 2015b; Leclercq 2015; Leclercq, Jasche & Wandelt 2015).

This paper is organized as follows. We first review the COLA algorithm, and describe our COLA simulations for the WiggleZ survey in Section 2, and compare our simulations with conventional *N*-body simulations in Section 3. We describe our mock galaxy catalogue based on COLA in Section 4, and compare the mock galaxies with those based on conventional simulations in Section 5. Throughout the paper, we use a flat Λcold dark matter cosmology with $\Omega_{\mathrm{m}} = 0.273$, $\Omega_{\Lambda} = 0.727$, $\Omega_{\mathrm{b}} = 0.0456$, $h = 0.705$, $\sigma_8 = 0.812$, and $n_{\mathrm{s}} = 0.961$, which is the *Wilkinson Microwave Anisotropy Probe* 5 cosmology (Komatsu et al. 2009) used for the Gigaparsec WiggleZ simulation Poole et al. (2015).

## 2 COLA SIMULATION

We use the COLA method invented by Tassev et al. (2013, TZE hereafter) to run many realisations of cosmological simulations with a reasonable amount of computation time. COLA enables a reduction in the number of time steps by combining second-order Lagrangian Perturbation Theory (2LPT) and *N*-body simulation.

### 2.1 Introduction to the COLA algorithm

A typical time-evolution method for *N*-body simulation is the leapfrog integration:

$$\boldsymbol{x}_{i+1} = \boldsymbol{x}_i + \boldsymbol{v}_{i+1/2}\Delta t \tag{1}$$

$$\boldsymbol{v}_{i+1/2} = \boldsymbol{v}_{i-1/2} + \boldsymbol{F}(\boldsymbol{x}_i)\Delta t, \tag{2}$$

where $\boldsymbol{x}_i$ ($i = 0, 1, 2, \ldots$) is the position of a particle at time $t_i \equiv i\Delta t$, $\boldsymbol{v}_{i+1/2}$ is the velocity at $t_{i+1/2} \equiv (i + 1/2)\ \Delta t$, and $F(\boldsymbol{x})$ is the acceleration at $\boldsymbol{x}$, for some time step $\Delta t$. [The equations are solely for illustrating the difference between the conventional leapfrog integration and COLA; terms for the expanding Universe are dropped. See, e.g. Quinn et al. (1997) for the leapfrog time stepping for cosmological simulations.] The leapfrog integration is accurate up to second order in $\Delta t$, but the truncation error from higher orders in $\Delta t$ makes the time evolution inaccurate for large $\Delta t$. In addition, the time step is usually proportional to the Hubble time $H^{-1}(t)$ to integrate accurately in cosmological simulations, which is smaller at higher redshifts. Since we can approximate the motion well by 2LPT at high redshifts, we can use larger time steps at high redshifts with COLA than the conventional leapfrog integration.

COLA has two techniques that improve the accuracy of time integration for large time steps. The first technique is using the discrete time evolution only for the non-linear terms beyond 2LPT, i.e. the residual particle position, velocity, and acceleration from their 2LPT contributions:

$$\boldsymbol{x}_{\mathrm{res}} \equiv \boldsymbol{x} - \boldsymbol{x}_{\mathrm{2LPT}}(t), \tag{3}$$

$$\boldsymbol{v}_{\mathrm{res}} \equiv \boldsymbol{v} - \dot{\boldsymbol{x}}_{\mathrm{2LPT}}(t), \tag{4}$$

$$\boldsymbol{F}_{\mathrm{res}} \equiv \boldsymbol{F}(\boldsymbol{x}) - \ddot{\boldsymbol{x}}_{\mathrm{2LPT}}(t), \tag{5}$$

where the dots are time derivatives, and,

$$\boldsymbol{x}_{\mathrm{2LPT}}(t) = \boldsymbol{q} + D_1(t)\boldsymbol{\Psi}^{(1)}(\boldsymbol{q}) + D_2(t)\boldsymbol{\Psi}^{(2)}(\boldsymbol{q}), \tag{6}$$

is the growing-mode solution of 2LPT, mapping the initial comoving position $\boldsymbol{q}$ to a later position at time $t$. The time evolution is given by the linear growth factor $D_1(t)$, and the second-order growth factor $D_2(t)$, which is approximately[1] $D_2(t) = -\frac{3}{7}D_1(t)^2\Omega(a(t))^{-1/143}$, where $\Omega(a) = \Omega_{\mathrm{m}}/(\Omega_{\mathrm{m}} + \Omega_{\Lambda}a^3)$ (see Bouchet et al. 1995; Bernardeau et al. 2002, and references therein for 2LPT). The first- and second-order motions are integrated analytically with 2LPT, which does not have the truncation error for discrete $\Delta t$.

The second technique is an ansatz that the residual velocity decays as,

$$\boldsymbol{v}^{\mathrm{res}}(t) = \boldsymbol{v}^{\mathrm{res}}_{i+1/2}\left(\frac{a(t)}{a(t_{i+1/2})}\right)^{n_{\mathrm{LPT}}} \tag{7}$$

for $t_i \le t \le t_{i+1}$ during a drift step $\boldsymbol{x}_i \mapsto \boldsymbol{x}_{i+1}$, and,

$$\boldsymbol{v}^{\mathrm{res}}(t) = A_i + B_i a(t)^{n_{\mathrm{LPT}}} \tag{8}$$

for $t_{i-1/2} \le t \le t_{i+1/2}$ during a kick step, $\boldsymbol{v}^{\mathrm{res}}_{i-1/2} \mapsto \boldsymbol{v}^{\mathrm{res}}_{i+1/2}$, where $A_i$ and $B_i$ are constants, $a$ is the scale factor, and $n_{\mathrm{LPT}}$ is a free parameter tuned to reproduce conventional *N*-body simulations most accurately. We use the value $n_{\mathrm{LPT}} = -2.5$ found by TZE, which gives the best cross-correlation coefficient between the true density field and the one produced by COLA. These functions replace the linear functions of $\Delta t$ in equations (1 and 2), and suppress the higher order terms. (Note that the growing mode is captured by 2LPT, and

[1] The public 2LPTic code (footnote 3), originally designed to generate initial conditions at high redshifts, does not contain the factor $\Omega^{-1/143}$, which is negligible at high redshift. We correctly include this factor. The effect, however, is negligible, only a sub-per cent contribution to the second order at all redshifts.

the residual term is a decaying mode – at least in the linear perturbation theory.) The two equations (7 and 8) are empirical, and not exactly consistent with each other; equation (7) is assuming that $A_i$ is negligible compared to the second term with $B_i$ in equation (8). In fact, TZE suggest another ansatz, $v^{\rm res}(t) = v^{\rm res}_{i+1/2}$, as a replacement for equation (7) for simulations starting at high redshift $z \sim 49$ with low-mass resolution, which is the other limit that $B_i a(t)^{n_{\rm LPT}}$ is negligible compared to $A_i$. The optimum ansatz, including the value of $n_{\rm LPT}$, depends on the redshift and resolution. 'Experimentation is always advised with COLA' (TZE).

### 2.2 Basic equations

We briefly review the equations of motion of dark matter particles in the expanding Universe, and then present the COLA time evolution equations (see also the original description by TZE). Let $\boldsymbol{x}$ be the comoving coordinate of an $N$-body particle, and $\boldsymbol{v} = a^2\dot{\boldsymbol{x}}$ be its canonical velocity. The canonical velocity, $\boldsymbol{v} = m^{-1}\partial L/\partial\dot{\boldsymbol{x}}$, follows from the Lagrangian,

$$L = \frac{1}{2}m(a\dot{\boldsymbol{x}})^2 - m\phi(\boldsymbol{x}, t), \tag{9}$$

where $m$ is the particle mass, $a\dot{\boldsymbol{x}}$ is the physical peculiar velocity, and $\phi$ is the peculiar gravitational potential that satisfies the Poisson equation in the physical coordinate $\nabla_{\rm phys} = \nabla/a$:

$$\left(\frac{1}{a}\nabla\right)^2 \phi(\boldsymbol{x}, t) = 4\pi G\left[\rho(\boldsymbol{x}, t) - \bar{\rho}(t)\right], \tag{10}$$

for the matter density $\rho$ and mean matter density $\bar{\rho}$. This can be written as

$$\nabla^2\phi(\boldsymbol{x}, t) = \frac{3}{2}H_0^2\Omega_{\rm m}a^{-1}(t)\delta(\boldsymbol{x}, t), \tag{11}$$

using the density contrast $\delta \equiv \rho/\bar{\rho} - 1$, the present critical density $\rho_{\rm crit,0} \equiv 3H_0^2/(8\pi G)$, Hubble constant $H_0$, and the present matter density $\Omega_m \equiv \bar{\rho}/\rho_{\rm crit,0}$. The Euler–Lagrange equation gives the equations of motion,

$$\dot{\boldsymbol{x}} = \boldsymbol{v}/a(t)^2, \tag{12}$$

$$\dot{\boldsymbol{v}} = m^{-1}\partial L/\partial\boldsymbol{x} = -\nabla\phi(\boldsymbol{x}, t) \equiv \boldsymbol{F}(\boldsymbol{x}, t). \tag{13}$$

We discretize the time into $n_{\rm step} = 10$ steps, uniformly in $a$ between scale factor 0 and 1,

$$a(t_i) = a_i \equiv i/n_{\rm step}, \tag{14}$$

$$a(t_{i+1/2}) = a_{i+1/2} \equiv (i + 1/2)/n_{\rm step} \tag{15}$$

and set the initial condition,

$$\boldsymbol{x}^{\rm res}(t_1) = 0, \qquad \boldsymbol{v}^{\rm res}(t_{1/2}) = 0, \tag{16}$$

which means that the position and the velocity are exactly equal to those of 2LPT. This is slightly different from TZE; they set the initial condition at $a = 0.1$ for both the position and the velocity, and divide the scale factor by 10 between 0.1 and 1. (Our time stepping is 'nine steps' in their language.) Even though setting the initial velocity at $t_{1/2}$ is natural for leapfrog integration, we find that this causes 2–3 per cent excess in the matter power spectrum at $k \sim 0.2\,h$ Mpc$^{-1}$; the original TZE initial condition may be more accurate. We present the results using the original initial condition in Appendix A.

The ansatz for the drift step (equation 7) and one of the equations of motion (equation 12) give,

$$\boldsymbol{x}^{\rm res}(t) = \boldsymbol{x}^{\rm res}_i + \boldsymbol{v}^{\rm res}_{i+1/2}\int_{t_i}^{t}\left(\frac{a(t')}{a_{i+1/2}}\right)^{n_{\rm LPT}}\frac{{\rm d}t'}{a(t')^2}, \tag{17}$$

for $t_i \le t \le t_{i+1}$. We compute the integral numerically, which is common for all particles. The time evolution during the kick step (equation 8) is

$$\boldsymbol{v}^{\rm res}(t) = \boldsymbol{v}^{\rm res}_{i-1/2} + \frac{a(t)^{n_{\rm LPT}} - a_{i-1/2}^{n_{\rm LPT}}}{n_{\rm LPT}\,a(t_i)^{n_{\rm LPT}-1}\,\dot{a}(t_i)}\boldsymbol{F}^{\rm res}(\boldsymbol{x}_i). \tag{18}$$

for $t_{i-1/2} \le t \le t_{i+1/2}$; the constants $A_i$ and $B_i$ in equation (8) are set by matching the velocity at $t = t_{i-1/2}$,

$$\boldsymbol{v}^{\rm res}(t_{i-1/2}) = \boldsymbol{v}^{\rm res}_{i-1/2}, \tag{19}$$

and the acceleration at $t = t_i$,

$$\dot{\boldsymbol{v}}^{\rm res}(t_i) = B_i n_{LPT}\,a(t_i)^{n_{\rm LPT}-1}\,\dot{a}(t_i) = \boldsymbol{F}^{\rm res}(x_i). \tag{20}$$

We use equations (17 and 18) to update the $N$-body particle positions and velocities $\boldsymbol{x}^{\rm res}_i \mapsto \boldsymbol{x}^{\rm res}_{i+1}$, $\boldsymbol{v}^{\rm res}_{i-1/2} \mapsto \boldsymbol{v}^{\rm res}_{i+1/2}$, and also to interpolate the quantities between time steps for snapshots at redshifts of our interest.

### 2.3 The WiggleZ COLA (WiZ-COLA) simulation

The WiggleZ-COLA (WiZ-COLA) simulation is a set of COLA simulations designed for the WiggleZ Dark Energy Survey (Drinkwater et al. 2010) to quantify the systematic and statistical errors in data analyses. We run 3600 COLA simulations with different initial random modes to generate 600 independent realisations of mock galaxies for six survey regions in the sky (we use six independent realisations for the six regions). The WiggleZ survey is a redshift survey which covers about 1000 deg$^2$ up to redshift 1. The survey volume consists of six regions in the sky, and analysed in three redshift bins $\Delta z^{\rm Near}$ ($0.2 < z < 0.6$), $\Delta z^{\rm Mid}$ ($0.4 < z < 0.8$), and $\Delta z^{\rm Far}$ ($0.6 < z < 1.0$). We use a periodic simulation box of $600\,h^{-1}$ Mpc on a side to cover any one of these redshift bins. The mass of dark matter haloes hosting the emission-line galaxies in the WiggleZ sample, inferred from the galaxy bias (Marín et al. 2013), is about $10^{12}\,h^{-1}\,{\rm M}_\odot$. We use $1296^3$ particles, which gives the particle mass $7.5 \times 10^9\,h^{-1}\,{\rm M}_\odot$, to have more than 100 particles for $10^{12}\,h^{-1}\,{\rm M}_\odot$ haloes. This mass resolution is equal to that of the Gigaparsec WiggleZ simulation (GiggleZ; Poole et al. 2015), which has $2160^3$ particles in a $1\ h^{-1}$ Gpc box on a side. We use $(3 \times 1296)^3$ meshes for Particle Mesh (PM) gravitational force solver to resolve haloes as TZE suggested.

We parallelize the publicly available serial COLA code[2] by TZE to run simulations that satisfy the volume and mass resolution required for the WiggleZ survey. We combine our parallelized COLA code with a 2LPT code, 2LPTIC,[3] based on N-GenIC,[4] and an FoF halo finder at $N$-body shop[5] for efficient on-the-fly generation of halo catalogues. We use a parallel Fast Fourier Transform library, FFTW3 (Frigo & Johnson 2005) for 2LPT and PM. We follow the slab decomposition of FFTW, which slices the volume along one axis. We divide the simulation cube into 216 equal-volume slices, and we move $N$-body particles between volumes after each time

[2] https://bitbucket.org/tassev/colacode/
[3] http://cosmo.nyu.edu/roman/2LPT/
[4] http://www.gadgetcode.org/
[5] http://www-hpcc.astro.washington.edu/tools/fof.html

**Table 1.** Computation wallclock time of each procedure in one COLA simulation using 216 cores.

| Procedure | Time (s) | Fraction % |
|---|---|---|
| 2LPT | 18 | 2 |
| FFT in COLA | 583 | 66 |
| Other processes in COLA | 114 | 13 |
| Data analysis (FOF) | 167 | 19 |
| Total | 882 | 100 |

step using the Message Passing Interface. We do not write all the dark matter particles to the hard drive, we only write haloes with more than 32 particles and the matter density field on a grid at redshifts 0.73, 0.6, 0.44, and 0. The first three redshifts are the effective redshifts of $\Delta z^{\rm Far}$, $\Delta z^{\rm Mid}$ and $\Delta z^{\rm Near}$, respectively.

We use 216 cores and 4 × 216 Gbytes of random access memory in the Green II supercomputer at Centre for Astrophysics and Supercomputing at Swinburne University. This number of cores is necessary to allocate the large mesh. In Table 1, we list the composition of the computation time for one realization; one realization takes about 15 min, and the majority of them (66 per cent) are used for the FFTW for gravity solving. Only 2 per cent of the time is used for 2LPT. Our COLA simulations are about a factor of 50 slower than 2LPT, but still more than 100 times faster than typical *N*-body simulations, which we describe in the following section.

## 3 ACCURACY OF COLA SIMULATION

To test the accuracy of our COLA simulations, we compare them with simulations performed with the same number of particles and the same initial random modes using the publicly available Tree-PM *N*-body code GADGET-2 (Springel 2005). For GADGET, we use $2592^3$ PM grids and a softening length equal to 5 per cent of the mean particle separation. We use the default values of accuracy parameters; $\eta = 0.025$ for the time step, and $\alpha = 0.005$ for the force accuracy. We setup the initial condition at $z = 49$ using the same 2LPT displacement fields. We make 14 realizations, and each of the *N*-body runs takes about 9000 CPU hours using 384 computing cores. The computation time for one realization is about 160 times larger than that for our COLA simulation.

### 3.1 Haloes in 2LPT, COLA and GADGET simulations

In Fig. 1, we show slices of 2LPT, COLA, and GADGET simulations at redshift 0.6. The red points are simulation particles in 'massive haloes' above $10^{13}\,h^{-1}\,{\rm M}_\odot$, and blue points are particles in 'low-mass haloes' in the range $10^{12}\,h^{-1}\,{\rm M}_\odot < M < 10^{13}\,h^{-1}\,{\rm M}_\odot$. We identify the haloes with the FoF algorithm with linking length 0.2 times the mean particle separation ($\ell = 0.2$) for GADGET and COLA, and $\ell = 0.37$ for 2LPT, following the prescription of PTHaloes by Manera et al. (2013). The halo masses are based on those of the GADGET simulation. The haloes in the COLA and 2LPT simulations are sorted by mass in descending order, and the haloes are classified as massive or low mass by the ranking. The massive PThaloes are found in approximately correct locations, but low-mass PThaloes are completely mislocated; haloes in filaments are not resolved, and the noise around massive haloes is incorrectly identified as low-mass haloes. The COLA simulation, on the other hand, is almost indistinguishable to the GADGET simulation; only a small number of haloes crosses the mass boundary of $M = 10^{13}h^{-1}$ due to a scatter in mass.

We can also see the problem of the PTHaloes in the halo bias. In Fig. 2, we plot the linear halo bias for haloes grouped by their masses. Each group has a number density $2.5 \times 10^{-4}(h^{-1}\,{\rm Mpc})^{-3}$, and the corresponding mass range is based on the GADGET simulation. The linear bias is computed by matching the amplitude of the halo power spectrum with the matter power spectrum of MPTBREEZE (Crocce, Scoccimarro & Bernardeau 2012) for $k \leq 0.1\,h^{-1}\,{\rm Mpc}$ (see more details in Section 3.3 for the power spectrum computation). The bias of PTHaloes is always above 2, because all the haloes are clustered around massive haloes. The biases of COLA haloes have correct dependence on mass, but are 5 per cent smaller than those of GADGET, which is probably due to the scatter in the halo mass. Since there are more low-bias haloes than high-bias haloes, the scatter introduces a larger fraction of low-bias haloes into the group.

### 3.2 Halo mass

In Fig. 3, we plot the halo masses of COLA and GADGET. For each halo in the COLA simulation, $H_{\rm COLA}$, we find the GADGET halo, $H_{\rm GADGET}$, that contains the largest number of halo particles in $H_{\rm COLA}$, $f$: $H_{\rm COLA} \mapsto H_{\rm GADGET}$, then we find the same mapping in the opposite direction for each GADGET halo, $g$: $H_{\rm GADGET} \mapsto H_{\rm COLA}$. In the figure, we plot the masses for a subset of halo pairs that the

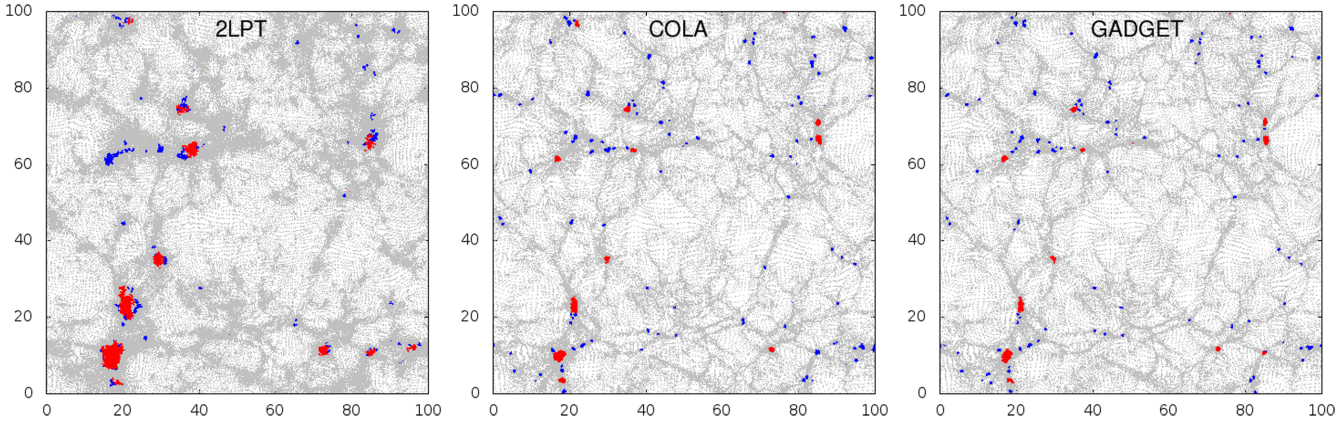


**Figure 1.** Simulation particles in 2LPT, COLA, and GADGET simulations, from left to right, respectively, in subvolumes of $100 \times 100 \times 2\,(h^{-1}\,{\rm Mpc})^3$. The red particles are particles in massive haloes, $M \geq 10^{13}\,h^{-1}\,{\rm M}_\odot$, and blue particles are in low-mass haloes, $10^{12}\,h^{-1}\,{\rm M}_\odot \leq M < 10^{13}\,h^{-1}\,{\rm M}_\odot$. 2LPT simulation can only resolve massive haloes, while COLA can resolve both massive and low-mass haloes.

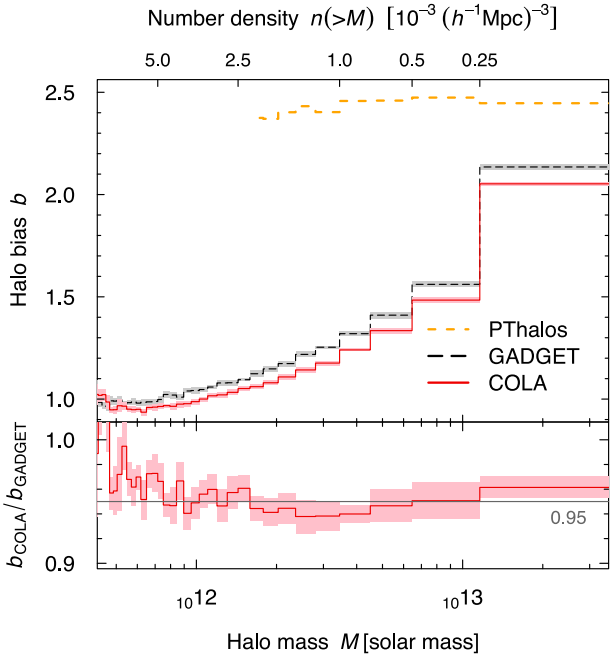


**Figure 2.** Linear biases of haloes grouped by their masses; each bin corresponds to a number density of $2.5 \times 10^{-4}(h^{-1}\,\mathrm{Mpc})^{-3}$. COLA haloes have correct bias with about 5 per cent accuracy, while PThalos have reasonable bias only for the most massive bin. (The errors are twice the standard errors in the mean of 14 realizations.)

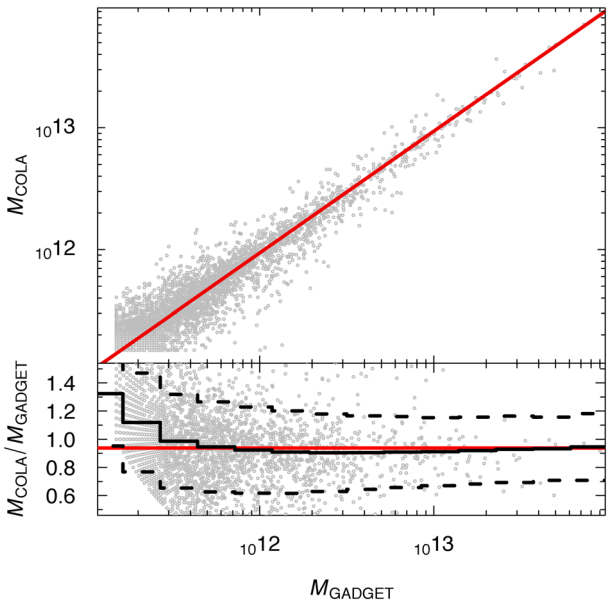


**Figure 3.** The relation of halo masses in the COLA simulation $M_{\mathrm{COLA}}$ and those in the GADGET simulation $M_{\mathrm{GADGET}}$. The straight red lines in both panels are the linear fit, $M_{\mathrm{COLA}} = 0.938\,M_{\mathrm{GADGET}}$. The solid and dashed black lines in the bottom panel are the mean and the standard deviation of the ratio $M_{\mathrm{COLA}}/M_{\mathrm{GADGET}}$, respectively. The ratios are almost mass independent, and the scatters are 0.25–0.30.

both mappings exist and point to each other: $\{(H_{\mathrm{COLA}}, H_{\mathrm{GADGET}})$: $f(H_{\mathrm{COLA}}) = H_{\mathrm{GADGET}}$ and $g(H_{\mathrm{GADGET}}) = H_{\mathrm{COLA}}\}$.

The linear fitting gives,

$$M_{\mathrm{COLA}} = 0.938 M_{\mathrm{GADGET}}. \quad (21)$$

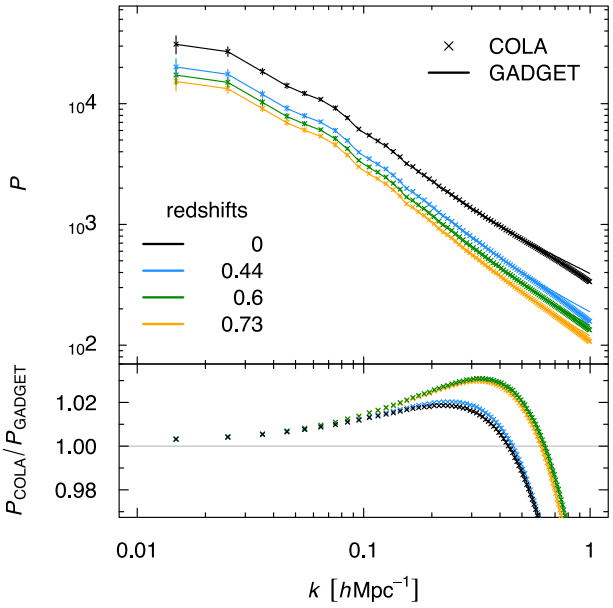


**Figure 4.** (Upper panel:) matter power spectra of a COLA simulation (points) and a GADGET simulation (lines) at $z = 0$, 0.44, 0.6 and 0.73, which have the same initial condition. (Lower panel:) ratios of COLA power spectra to those of GADGET.

The ratio $M_{\mathrm{COLA}}/M_{\mathrm{GADGET}}$ is almost independent of mass, except below $10^{12}\,h^{-1}\,\mathrm{M}_{\odot}$ where the artificial increase in the ratio is caused by the minimum halo mass of 32 particles per halo. The scatters in the ratios are about 0.24 above $10^{13}\,h^{-1}\,\mathrm{M}_{\odot}$, and increase to about 0.3 near $10^{12}\,h^{-1}\,\mathrm{M}_{\odot}$.

### 3.3 Matter power spectrum

We compare the matter power spectra of COLA with those of GADGET in Fig. 4 for the 14 realizations with same initial conditions. COLA is accurate within 1.4 per cent for $k \leq 0.1\,h\,\mathrm{Mpc}^{-1}$ and 2.5 per cent for $k \leq 0.2\,h\,\mathrm{Mpc}^{-1}$, respectively. The error bars are twice the standard error in the mean,

$$\Delta P \equiv 2\sigma(P)/\sqrt{N_{\mathrm{r}}}, \quad (22)$$

where $\sigma(P) = \sum_{i=1}^{N_{\mathrm{r}}}(P_i - \bar{P})^2/(N_r - 1)$ is the standard deviation, $\bar{P} = \sum_{i=1}^{N_{\mathrm{r}}} P_i/N_{\mathrm{r}}$ is the mean, and $N_{\mathrm{r}} = 14$ is the number of the realisations. The error bars for the ratio in the bottom panel are too small to see; cosmic variance does not directly affect the ratio of two simulations using the same initial modes. We find an excess in the power spectrum ratio, $P_{\mathrm{COLA}}/P_{\mathrm{GADGET}} > 1$, which was not seen in the original paper (TZE); this is caused by the slight difference in the initial condition (equation 16, see also Appendix A). The amount of error seems to fall into two groups; a group of redshifts 0 and 0.44, and the other group of 0.60 and 0.73. This could be due to our interpolation between time steps (equation 17). Redshifts 0 and 0.44 correspond to scale factor 1 and 0.694 which are close to the drift steps (equation 14), while the latter group with slightly larger errors is offset from the scale factor steps by about 0.025. There is probably room for a small improvement in the interpolation formula by adding a term that uses the acceleration.

In Fig. 5, we plot the mean matter power spectrum of 3600 realizations and compare with an analytical power spectrum from MPTBREEZE (Crocce et al. 2012). The long-wavelength modes, $k \leq 0.1\,h\,\mathrm{Mpc}^{-1}$ are accurate within the statistical uncertainty; the $\chi^2$ for the first nine data points, $k \leq 0.1\,h\,\mathrm{Mpc}^{-1}$, is 7.1. We use a

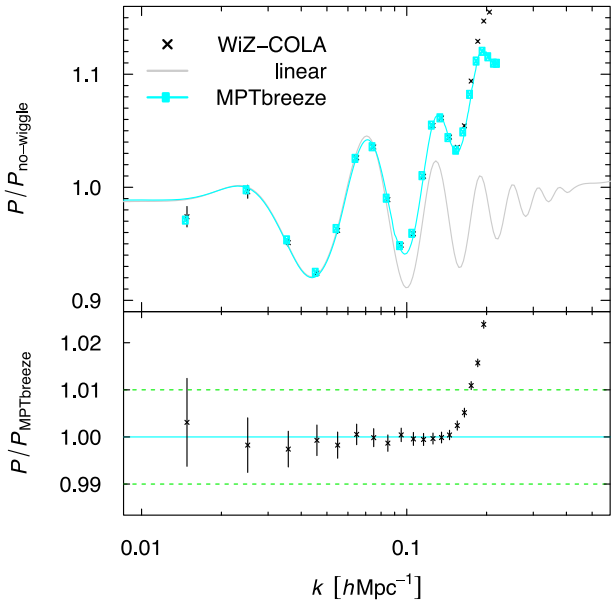


**Figure 5.** (Upper panel:) mean matter power spectrum of 3600 COLA simulations (WiZ-COLA, black crosses) compared to a non-linear analytical power spectrum by MPTbreeze (cyan line) at $z = 0.6$. Cyan circles are the analytical power spectrum averaged on discrete grids in Fourier space. (Lower panel:) the ratio of WiZ-COLA power spectrum to the analytical power spectrum, both averaged on the same discrete grid in Fourier space. COLA simulations give very accurate overall amplitude, in agreement with the analytical power spectrum within statistical fluctuation. (The error bars are twice the standard errors in the mean.)

publicly available code[6] (Taruya et al. 2012) for the reference 'no-wiggle' power spectrum (Eisenstein & Hu 1998). The good match between COLA and MPTbreeze near $k = 0.1\ h\,\mathrm{Mpc}^{-1}$ is partially due to a coincidence, as we see errors larger than 1 per cent in Fig. 4; the accuracy of MPTbreeze is about 2 per cent on BAO scales, $k \lesssim 0.1\ h\,\mathrm{Mpc}^{-1}$. Here, we highlight the accuracy in the linear growth factor in the matter power spectrum, which is a benefit of using 2LPT in COLA; 10-time step PM simulations, with conventional leapfrog integration alone, have 1–2 per cent error in the overall power spectrum amplitude (TZE).

The detail of calculating the power spectrum is as follows. We assign matter densities on $324^3$ grids using the Cloud in Cell assignment, using all dark matter particles on the fly, and compute the density contrast in Fourier space, $\delta(\boldsymbol{k})$, using a Fast Fourier Transform. The FFTW library provides discrete $\delta(\boldsymbol{k})$ for $k_z \geq 0$ – modes in the other half of the Fourier space do not contain independent information due to the reality condition $\delta(-\boldsymbol{k}) = \delta(\boldsymbol{k})^*$. To avoid double counting of modes on the $k_z = 0$ plane, we use the modes $\{k_z > 0\} \cup \{k_z = 0 \text{ and } k_y > 0\} \cup \{k_z = 0 \text{ and } k_y = 0 \text{ and } k_x > 0\}$. We compute the averages $P(k) = V^{-1}\langle\delta(\boldsymbol{k})\delta^*(\boldsymbol{k})\rangle$ and plot against the average wavenumbers $\langle k\rangle$ in bins of a fixed width $\Delta k_{\rm bin} = 0.01\,h$ Mpc$^{-1}$, where $V$ is the volume of the simulation box. The average $\langle P\rangle$ is not an unbiased estimate of $P(\langle k\rangle)$ in general; $P(\langle k\rangle) = \langle P(k)\rangle$ is guaranteed only if $P(k)$ is a linear function of $k$ within the bin. We, therefore, average the analytical power spectra on the same discrete three-dimensional grid for accurate comparison, which are plotted by cyan circles in Fig. 5. This discrete averaging makes statistically significant differences, especially between $k = 0.01$ and $0.02\ h\,\mathrm{Mpc}^{-1}$, where the power spectrum deviates significantly from a linear function, reaching the maximum and turning over. We correct for the smoothing and the aliasing effect using the procedure by Jing (2005).

[6] http://www2.yukawa.kyoto-u.ac.jp/~atsushi.taruya/cpt_pack.html

## 4 MOCK GALAXY CATALOGUES

We populate the haloes with mock galaxies using the Halo Occupation Distribution (HOD) prescription.

### 4.1 HOD for WiggleZ galaxies

We use a lognormal HOD (Zehavi et al. 2005; Cai, Bernstein & Sheth 2011) for the emission-line galaxies in the WiggleZ sample. We assume that the probability that a dark matter halo of mass $M$ hosts a WiggleZ galaxy is,

$$P(M) = \exp\left[-\frac{(\log_{10} M - \log_{10} M_0)^2}{2\sigma^2_{\log M}}\right], \tag{23}$$

where $\log_{10} M_0$ and $\sigma_{\log M}$ are parameters fitted against data. We populate at most one galaxy per halo, without any satellite galaxies, and set the position and velocity of the galaxy equal to the averages of the host halo particles (i.e. the centre-of-mass position and velocity). We do not use the error function HOD (Zheng et al. 2005), because we do not expect to find emission-line galaxies, which are young star-forming galaxies, in groups or clusters hosted by massive haloes.

We find the two HOD parameters by matching the projected correlation function,

$$w_p(r_p) = \int_{-\pi_{\rm max}}^{\pi_{\rm max}} \xi(r_p, \pi)\mathrm{d}\pi, \tag{24}$$

with $\pi_{\rm max} = 60\,h^{-1}$ Mpc. We perform the matching by populating a series of mock catalogues using a trial set of HOD parameters, computing the mock mean, and comparing the mock mean with the data by minimizing a $\chi^2$ statistic using a covariance matrix obtained from jack-knife re-sampling. Since $\log M_0$ and $\sigma_{\log M}$ are degenerate, we fix $\sigma_{\log M} = 0.1$. We find $\log_{10} M_0 = 12.17$ for $\Delta z_{\rm Near}$ and $\Delta z_{\rm Far}$, and 12.28 for $\Delta z_{\rm Mid}$ for FoF halo mass $M$ without any corrections (Table 2, all masses are in units of $h^{-1}\,\mathrm{M}_\odot$). COLA halo mass is about 7 per cent smaller than true $N$-body simulation mass, but any constant calibration factor for the mass only rescales the parameters without any change in the HOD mock.

We subsample the HOD galaxies by a realization-independent factor to match the smooth number density without clustering $\bar{n}(\boldsymbol{x})$ using the survey selection function (Blake et al. 2010). At low redshift, there are rare cases that the number of HOD galaxies is not sufficient. In such cases, we increase the width of the HOD $\sigma_{\log M}$ for $M < M_0$ to match the number density, keeping the HOD the same for $M > M_0$.

### 4.2 HOD for BOSS CMASS galaxies

We also generate mock catalogues for the BOSS CMASS galaxies in the BOSS-WiggleZ overlap volume using the same simulation for the multitracer analyses (Beutler et al. 2016; Marín et al. 2016). We refer the reader to these papers for the detail of the overlap regions.

**Table 2.** Best-fitting HOD parameters. Masses are in units of $h^{-1}\,\mathrm{M}_\odot$.

| | WiggleZ | | | | BOSS | | | |
|---|---|---|---|---|---|---|---|---|
| | $\log_{10} M_0$ ($\Delta z^{\rm Near}$) | $\log_{10} M_0$ ($\Delta z^{\rm Mid}$) | $\log_{10} M_0$ ($\Delta z^{\rm Far}$) | $\sigma_{\log M}$ | $\log_{10} M_{\rm min}$ | $\sigma_{\log M}$ | $M_0$ | $\beta$ |
| COLA | 12.17 | 12.28 | 12.17 | 0.1 | 12.92 | 0.31 | 14.07 | 1.60 |
| GADGET | | 12.28 | | 0.1 | 12.92 | 0.37 | 14.00 | 1.45 |

We use the error function for the central galaxies, and a power law for the satellite galaxies. We populate at most one central galaxy per halo with a probability,

$$P(M) = \frac{1}{2}\left[1 + \mathrm{erf}\left(\frac{\log_{10} M_{200,m} - \log_{10} M_{\rm min}}{\sigma_{\log M}}\right)\right], \quad (25)$$

where $M_{200,\,\mathrm{m}}$ is a halo mass defined by the mass within a sphere of radius $r_{200,\,\mathrm{m}}$, whose mean overdensity is 200 times the mean matter density. We denote the similar quantities for 200 times the critical density with $M_{200,\,\mathrm{c}}$ and $r_{200,\,\mathrm{c}}$. If the halo has a central galaxy, we draw a number of satellite galaxies from a Poisson distribution with mean,

$$\langle M_{\rm sat}\rangle = (M_{200,\mathrm{m}}/M_0)^{\beta}. \quad (26)$$

A satellite HOD with an additional parameter, $[(M - M_1)/M_0]^{\alpha}$ (Zheng et al. 2005), is also used frequently, but $M_1$ is usually not sensitive to the clustering data, and does not significantly improve the fit (Blake, Collister & Lahav 2008).

We add a random offset and a random virial velocity to the satellite galaxy assuming a spherical Navarro, Frenk & White (1997) profile,

$$\rho(r) = \frac{\rho_0}{(r/r_{\rm s})(1 + r/r_{\rm s})^2}. \quad (27)$$

We can uniquely determine the two-parameter profile by specifying the mass $M_{200,\,\mathrm{c}}$ and a concentration parameter $c_{200,\,\mathrm{c}} = r_{200,\,\mathrm{c}}/r_{\rm s}$. We draw a random concentration parameter from a known relation in the literature, but there are several trivial steps to convert the halo mass to an appropriate one.

(i) We first set the FoF halo mass $M_{\rm FOF} = 1.066\,M_{\rm COLA}$, which is based on our calibration between COLA and GADGET simulations (Fig. 3);

(ii) compute the typical concentration factor $\bar{c}$ for mass $M_{\rm FOF}$ using Prada et al. (2012), but the relation is given as a function of $M_{200,\,\mathrm{c}}$;

(iii) convert the FoF mass halo to $M_{200,\,c}$ using Lukić et al. (2009), which depends on FoF mass and the concentration parameter. Their formula also corrects for the resolution effect for a small number of halo particles: $N_{200,\,\mathrm{c}} \equiv M_{200,\,\mathrm{c}}/m$, where $m$ is the particle mass;

(iv) start from an initial guess of $M^{(0)}_{200,\mathrm{c}} = M_{\rm FoF}$, and solve steps (ii) and (iii) iteratively for mean concentration $\bar{c}$,

$$\bar{c}^{(i+1)}_{200,\mathrm{c}} = \bar{c}_{200,\mathrm{c}}(M^{(i)}_{200,\mathrm{c}}), \quad (28)$$

$$M^{(i+1)}_{200,\mathrm{c}} = M_{200,\mathrm{c}}(M_{\rm FoF}, N^{(i)}_{200,\mathrm{c}}, \bar{c}^{(i+1)}_{200,\mathrm{c}}), \quad (29)$$

which converge quickly within several iterations;

(v) draw a random concentration parameter, $\log_{10} c_{200,\,\mathrm{c}}$ from a Gaussian distribution of mean $\log_{10}\bar{c}_{200,\mathrm{c}}$ and standard deviation $\sigma_{\log c} = 0.078$ (Manera et al. 2013);

(vi) recompute the mass $M_{200,\,\mathrm{c}}$ using the generated $c_{200,\,\mathrm{c}}$. This determines the halo profile completely, and we can compute $M_{200,\,\mathrm{m}}$ from the profile;

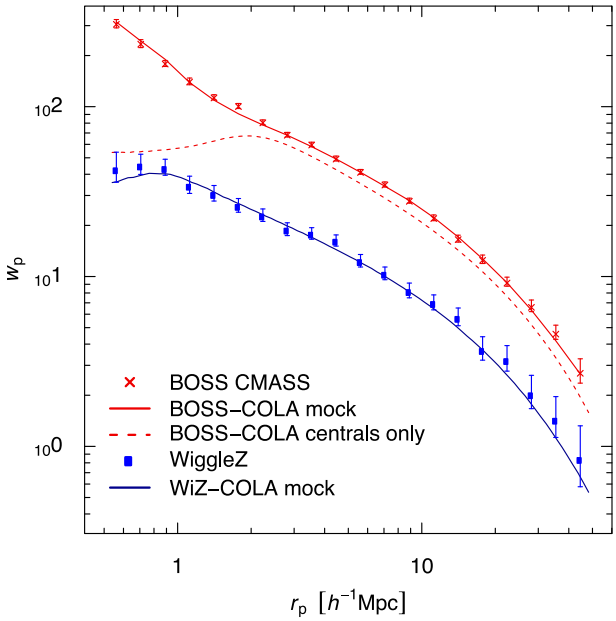


**Figure 6.** We tune the HOD parameters to match the projected correlation functions $w_{\rm p}$. The mock measurement agree with the data within the uncertainties. (The error bars for the data are $1\sigma$.)

(vii) draw the number of central and satellite galaxies for given HOD parameter using $M_{200,\,\mathrm{m}}$;

(viii) draw satellite positions from the static, spherical symmetric NFW profile from the phase-space distribution function. The static distribution function is uniquely determined from the density profile, assuming spherical symmetry and isotropic velocity distribution (Kazantzidis, Magorrian & Moore 2004).

We generate mocks for a grid of parameters, and find that $\log_{10} M_{\rm min} = 12.92$, $\sigma_{\log M} = 0.31$, $\log_{10} M_0 = 14.07$, and $\beta = 1.60$, fit the projected correlation function well. We also tried a concentration parameter relation by Bullock et al. (2001) with no additional scatter, but this made little difference.

In Fig. 6, we plot the projected correlation functions for the mock and the data. The solid lines are the mean of 3600 realizations generated in the periodic box. The log-normal HOD without satellite galaxies fits the WiggleZ data well, while a small contribution from satellites may improve the fit for $r \simeq 0.7h^{-1}$ Mpc. The BOSS CMASS clustering galaxies clearly requires satellite galaxies for $r \simeq 2h^{-1}$ Mpc.

### 4.3 Box remapping

We analyse the galaxy sample in three redshift bins, but the length along the line of sight is still larger than the box size. We rotate the simulation box to fit the volume with minimum overlap, using the box remapping technique (Carlson & White 2010) as a guide.

**Table 3.** Two box configurations that we use to remap the cubic simulation box to cuboids, which are characterized by three integer vectors, $u_i$ (Carlson & White 2010). $L_i$ are the lengths of three sides of the cuboid after remapping.

| Name | $\boldsymbol{u}_1$ | $\boldsymbol{u}_2$ | $\boldsymbol{u}_3$ | $L_1$ ($h^{-1}$ Mpc) | $L_2$ ($h^{-1}$ Mpc) | $L_3$ ($h^{-1}$ Mpc) |
|---|---|---|---|---|---|---|
| $\sqrt{2}$ | (1, 1, 0) | (1, 0, 1) | (1, 0, 0) | 848.5 | 734.8 | 346.4 |
| $\sqrt{3}$ | (1, 1, 1) | (1, 0, 0) | (0, 1, 0) | 1039.2 | 489.9 | 424.3 |

Their publicly available code[7] provides a list of possible remappings from a periodic cube to cuboids. We use two configurations, which we call $\sqrt{2}$ and $\sqrt{3}$, depending on the size of the volume (Table 3). The lengths of the remapped cuboid along the line of sight are, $L_1 = \sqrt{2}L = 849\,h^{-1}$ Mpc, and $L_1 = \sqrt{3}L = 1039\,h^{-1}$ Mpc, respectively, where $L = 600h^{-1}$ Mpc is the length of our simulation box on a side. In the table, we list the size of the cuboid after remapping, and the integer vectors $\boldsymbol{u}_i$, which characterize the remapping. The integer vectors specify the orthonormal basis of the remapped coordinate, $\boldsymbol{e}_i$, as follows:

$$\boldsymbol{e}_1 = \boldsymbol{u}_1/|\boldsymbol{u}_1|$$
$$\boldsymbol{e}_2 = \boldsymbol{u}_2'/|\boldsymbol{u}_2'|, \quad \boldsymbol{u}_2' \equiv \boldsymbol{u}_2 - (\boldsymbol{u}_1 \cdot \boldsymbol{u}_2/|\boldsymbol{u}_1|^2)\boldsymbol{u}_1,$$
$$\boldsymbol{e}_3 = \boldsymbol{e}_1 \times \boldsymbol{e}_2. \tag{30}$$

The basis vector $\boldsymbol{e}_1$ points the line of sight, $\boldsymbol{e}_2$ points the declination, and $\boldsymbol{e}_3$ points the Right Ascension directions, respectively, at the centres of the six survey regions. We use the cuboid $\sqrt{3}$ for $\Delta z^{\rm Near}$, which has enough length along the line of sight to fit the redshift range 0.2–0.6, and use $\sqrt{2}$ for $\Delta z^{\rm Mid}$ and $\Delta z^{\rm Far}$ when we need a wider cuboid in transverse directions. A small fraction of the survey volume was larger than the remapped cuboid, and the same volume in the simulation box was used twice. The fraction of such volume is 1.7 per cent of the total volume. In Table B1, we list the remapping we use and the fraction of overlap for each region.

### 4.4 Mock catalogue

The overall procedure for creating a mock catalogue from a halo catalogue is as follows.

(i) We fill the space with periodic replications of the simulation box, and rotate the positions and velocities to the remapped coordinate using the orthonormal basis (equation 30);

(ii) apply the redshift space distortion to the halo position:

$$\boldsymbol{s} = \boldsymbol{x} + \frac{\boldsymbol{v}\cdot\hat{\boldsymbol{x}}}{aH}\hat{\boldsymbol{x}}, \tag{31}$$

where $H$ is the Hubble parameter at scale factor $a$, and $\hat{\boldsymbol{x}} = \boldsymbol{x}/|x|$ is the unit vector parallel to $\boldsymbol{x}$;

(iii) populate the haloes with mock galaxies using the HOD (which may depend on the redshift-space position at low redshift to match the high number density);

(iv) subsample the mock galaxies to match the selection function (mask) of the survey. The subsample fraction is calculated to match the observed number of galaxies as a mean. The numbers of mock galaxies fluctuate around the observed number.

For the BOSS mock, we first generate the HOD galaxies and then apply the redshift-space distortions including the satellite virial velocities. We can interchange the step (ii) and (iii) because we use a position-independent HOD parameters for the BOSS galaxies. In Fig. 7, we plot slices of our WiZ-COLA mock catalogues for the 15 h region.

[7] http://mwhite.berkeley.edu/BoxRemap/

## 5 ACCURACY OF HOD GALAXIES

We test the accuracy of our mocks by comparing the HOD galaxies generated from COLA with the HOD galaxies generated from GADGET $N$-body simulations. We generate HOD galaxies in the periodic simulation box and compute the power spectra. We use the HOD parameters described in the previous section for the COLA HOD galaxies, but we determine different HOD parameters for the GADGET haloes to match the COLA power spectra in real space, because HOD parameters are free-fitting parameters that are usually adjusted for the observed galaxies (Table 2). If we used the same HOD parameters and the halo mass relation (equation 21), we would get about 5 per cent higher galaxy power spectrum from GADGET haloes as we see in Section 3.

In Fig. 8, we plot the power spectra in real and redshift space. We compute the monopole ($\ell = 0$) and the quadrupole ($\ell = 2$) moments for the redshift-space power spectrum $P^s$,

$$P^s_\ell(k) = \frac{2\ell+1}{2}\int_{-1}^{1} P_\ell(\mu)P^s(k,\mu)d\mu, \tag{32}$$

where $P_\ell$ is the Legendre polynomial, and $\mu = \hat{\boldsymbol{k}}\cdot\boldsymbol{e}_3$ is the consine of the angle between the wave vector and the fixed direction of the redshift-space distortion, $\boldsymbol{e}_3$, which is set to the direction of the third axis. The procedure of computing the power spectra is the same as that in Section 3.1; the only difference is that we also subtract the shot noise (Jing 2005).

In the lower panels, we plot the ratio of the power spectra. Although the HOD galaxies are based on simulations with the same initial condition, the ratio of the power spectra is affected by the randomness in populating the haloes with galaxies. The error bars are $2\sigma$ of the mean (equation 22) based on 14 realizations. The real-space power and the redshift-space monopole are very accurate; the ratios are consistent with unity for $k \leq 0.2\,h$ Mpc$^{-1}$ within the statistical fluctuation, and the statistical error is about 1 per cent.

Since we do not have enough statistics for the quadrupole moment for precise comparison, we also compute the cross-power spectra, $P_{\rm gu}$, and auto-power spectra, $P_{\rm uu}$, between the galaxy density and the line-of-sight peculiar velocity $u \equiv v_3/(aH)$, to show the accuracy of the peculiar velocities. The unit is converted to $h^{-1}$ Mpc, which corresponds to the displacement in redshift-space (equation 31). We use the nearest particle method to compute the velocity power spectrum; for each point of a regular grid, we assign the velocity of the nearest mock galaxy to the grid point (Zheng et al. 2013; Koda et al. 2014). This method gives a volume-weighted sample of the velocity field.

The redshift-space distortion is an effect of peculiar velocity, and the power spectrum in redshift space, $P^s$, is approximately

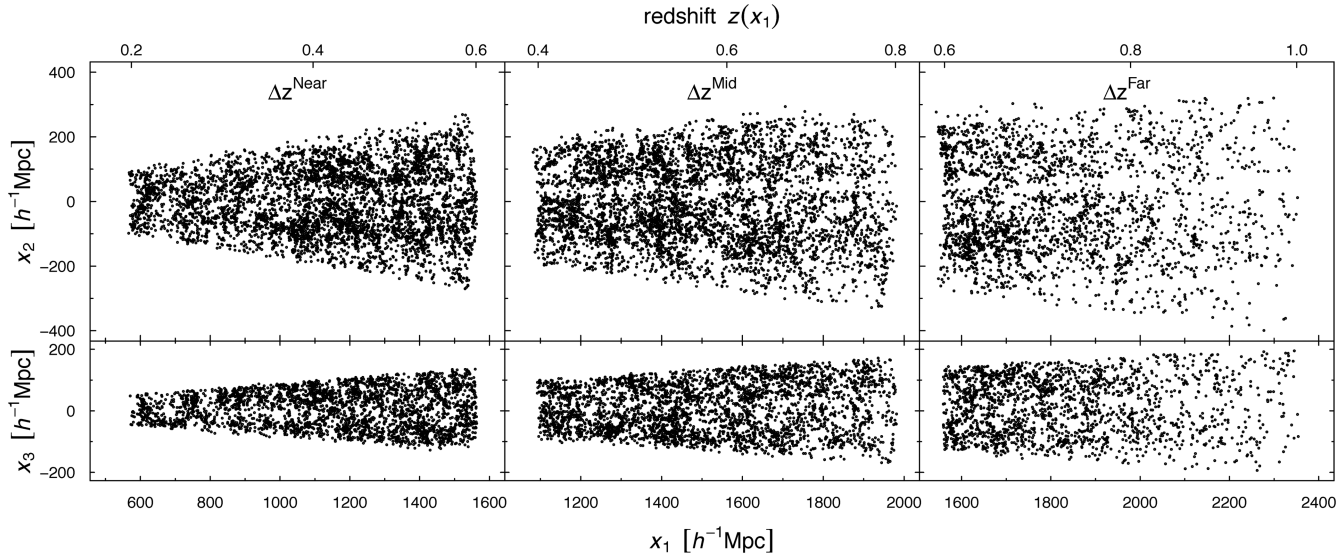


**Figure 7.** One realization of the mock galaxy catalogues for the 15 h region. The depth of the slices is $50\,h^{-1}$ Mpc. The coordinates are those of the remapped system, $x_i = \boldsymbol{x} \cdot \boldsymbol{e}_i$, whose origin $\boldsymbol{x} = 0$ is the observer.

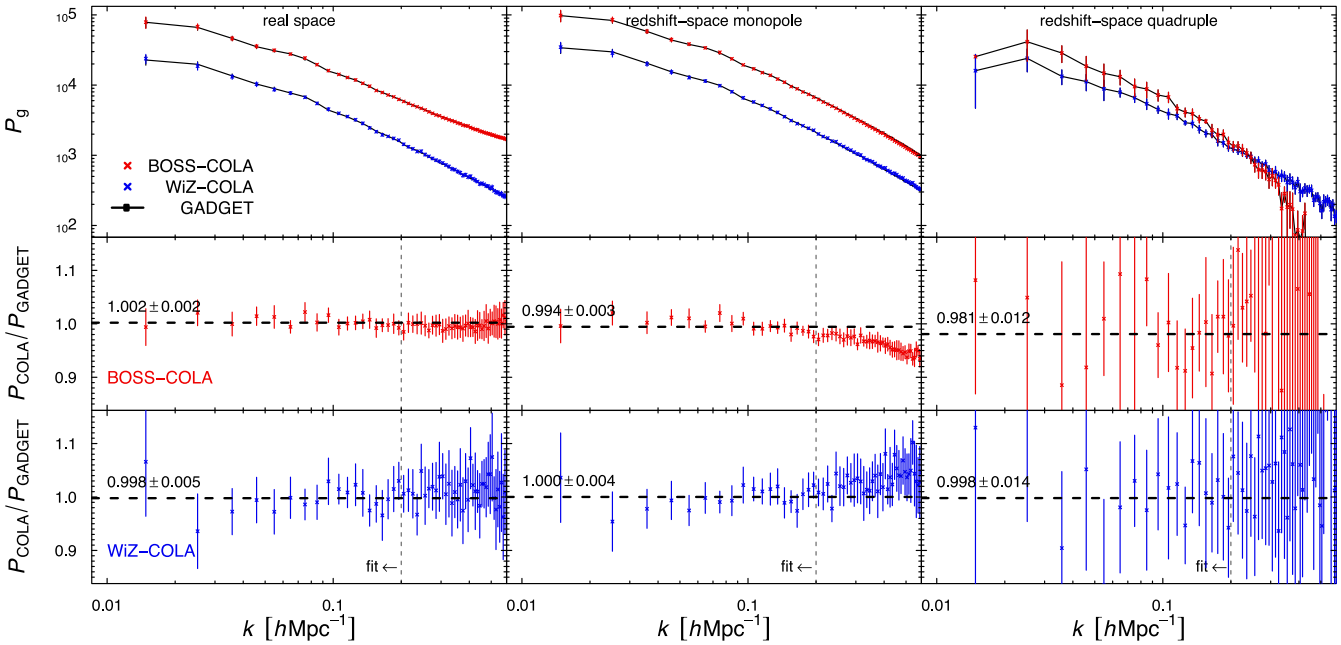


**Figure 8.** HOD galaxy power spectra generated from COLA versus GADGET in real and redshift space. COLA HOD galaxies show good agreement with the GADGET HOD galaxies. The horizontal lines in the power spectra ratios are the results of minimum $\chi^2$ fitting, based on the diagonal errors in the ratio from 14 realizations. The uncertainties in the fitting are 95-per cent intervals.

related to the galaxy density and velocity power spectra in real space (Appendix B),

$$P^{\rm s}(k,\mu) \approx P_{\rm gg}(k) + 2k\mu {\rm Im} P_{\rm gu}(k,\mu) + (k\mu)^2 P_{\rm uu}(k,\mu). \quad (33)$$

In Fig. 9, we plot the angle-averaged cross- and auto-power spectra, $\int_0^1 P_{\rm gu}(k,\mu)d\mu$ and $\int_0^1 P_{\rm uu}(k,\mu)d\mu$. The cross-power spectra are also accurate with about 1 per cent scatter, but the velocity–velocity power spectra for haloes (BOSS central galaxies and WiggleZ galaxies) have about 3 per cent error for $k \sim 0.1\,h$ Mpc$^{-1}$, and 5 per cent error for $k \geq 0.2\,h$ Mpc$^{-1}$. The BOSS satellite galaxies add additional error due to different virial velocities caused by different HOD parameters; this discrepancy of about 10 per cent shows that the velocity power spectrum is sensitive to HOD parameters, in general, through the non-linear random velocities, and is not necessarily a failure of the COLA mocks.

A good agreement in the real-space power spectrum is not difficult to achieve by tuning the HOD parameters or non-linear biasing models for haloes, but such tuning does not usually work simultaneously in redshift space. Faster mock generation techniques that uses 2LPT usually have about 5 per cent error in the monopole and 10 per cent error in the quadrupole of the redshift-space power spectrum (Chuang et al. 2015b). The primary advantage of COLA over 2LPT-based methods is the accuracy in the non-linear peculiar velocity, which may be important for the error evaluation of BAO reconstruction, and measurement of the growth rate. The accurate peculiar velocity is limited to that for haloes, and we do not expect accurate densities or virial velocities inside haloes. We find

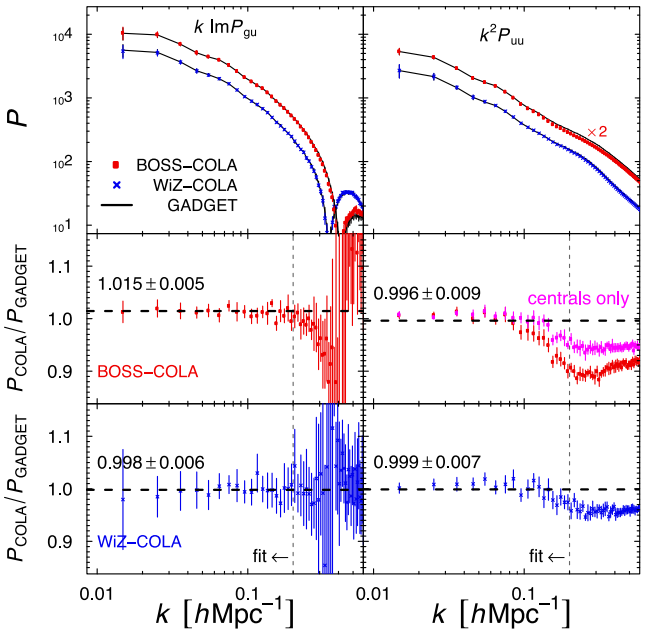


**Figure 9.** The cross- and auto-power spectra of HOD galaxy density and line-of-sight peculiar velocity. BOSS $P_{uu}$ is shifted by a factor of 2 to avoid overlap. COLA has accurate peculiar velocities. We do not find systematic error in the velocity-galaxy cross-power for $k \leq 0.2\,h\,\mathrm{Mpc}^{-1}$ and in the velocity auto-power for $k \leq 0.15\,h\,\mathrm{Mpc}^{-1}$; there are errors of about 3–5 per cent in the range $0.15\,h\,\mathrm{Mpc}^{-1} \leq k \leq 0.5\,h\,\mathrm{Mpc}^{-1}$.

discrepancies of 10 per cent at $k = 0.1\,h\,\mathrm{Mpc}^{-1}$, and 20 per cent at $k = 0.2\,h\,\mathrm{Mpc}^{-1}$, respectively, in redshift-space power spectra for $N$-body particles between COLA and GADGET, which seem to be consequences of inaccurate virial velocities inside the haloes.

Ideally we would like to compare the accuracy of the covariance matrix, since the main purpose of generating multiple realizations of mock catalogues is to compute covariance, but we do not have enough GADGET $N$-body simulations for covariance matrices. We do not have enough realisations to compare the two-point correlation function precisely, either. We leave these comparisons for future studies. We also note that we have tested the accuracy of COLA simulations against GADGET simulations with the same box size and mass resolution.

## 6 CONCLUSION

(i) We have presented the WiZ-COLA simulation, which consists of 3600 simulations with $1296^3$ particles that covers the volume of $(600\,h^{-1}\,\mathrm{Mpc})^3$, and resolve haloes of mass $10^{12}\,h^{-1}\mathrm{Mpc}$, using our new parallelized COLA code. The simulation took only 200 k core hours in total.

(ii) We generate 600 realizations of mock galaxy catalogues for the WiggleZ survey, and the BOSS CMASS galaxies in the overlap regions using HODs. We show that COLA can create mock HOD galaxies as accurate as GADGET $N$-body simulations for large-scale power spectra for wavelength $k \leq 0.2\,h\,\mathrm{Mpc}^{-1}$, both in real- and redshift-space.

(iii) The accuracy in peculiar velocity is the primary advantage of COLA simulations. We show that velocity power spectra are accurate within a per cent for $k \leq 0.15\,h\mathrm{Mpc}$ and 3 per cent for $0.2\,h\,\mathrm{Mpc}$, and we expect a similar accuracy for the quadrupole moment of the galaxy power spectra in redshift space. The accuracy of the galaxy-velocity cross-power spectra and monopole moment of galaxy power spectra is better than 1 per cent.

## ACKNOWLEDGEMENTS

We thank the anonymous referee for a careful reading of our paper. We thank Svetlin Tassev, Román Scoccimarro, Volker Springel, and their collaborators for making their codes public; our work was not possible without their public codes. This research was conducted by the Australian Research Council Centre of Excellence for All-sky Astrophysics (CAASTRO), through project number CE110001020. JK also acknowledges support of the European Research Council through the Darklight ERC Advanced Research Grant (#291521). CB acknowledges the support of the Australian Research Council through Future Fellowship awards FT110100639. Our numerical computation was supported by the gSTAR national facility at Swinburne University of Technology, the Flagship Allocation Scheme of the NCI National Facility at the ANU, and the Texas Advanced Computing Center (TACC) at The University of Texas at Austin. gSTAR is funded by Swinburne and the Australian Governments Education Investment Fund.

## REFERENCES

Amendola L. et al., 2013, Living Rev. Relativ., 16, 6
Anderson L. et al., 2012, MNRAS, 427, 3435
Anderson L. et al., 2014, MNRAS, 441, 24
Angulo R. E., Baugh C. M., Frenk C. S., Lacey C. G., 2014, MNRAS, 442, 3256
Avila S., Murray S. G., Knebe A., Power C., Robotham A. S. G., Garcia-Bellido J., 2015, MNRAS, 450, 1856
Bernardeau F., Colombi S., Gaztañaga E., Scoccimarro R., 2002, Phys. Rep., 367, 1
Beutler F. et al., 2012, MNRAS, 423, 3430
Beutler F., Blake C., Koda J., Marín F. A., Seo H.-J., Cuesta A. J., Schneider D. P., 2016, MNRAS, 455, 3230
Blake C., Collister A., Lahav O., 2008, MNRAS, 385, 1257
Blake C. et al., 2010, MNRAS, 406, 803
Blake C. et al., 2011, MNRAS, 418, 1707
Bouchet F. R., Colombi S., Hivon E., Juszkiewicz R., 1995, A&A, 296, 575
Bullock J. S., Kolatt T. S., Sigad Y., Somerville R. S., Kravtsov A. V., Klypin A. A., Primack J. R., Dekel A., 2001, MNRAS, 321, 559
Burrage C., Parkinson D., Seery D., 2015, preprint (arXiv:1502.03710)
Cai Y.-C., Bernstein G., Sheth R. K., 2011, MNRAS, 412, 995
Carlson J., White M., 2010, ApJS, 190, 311
Chuang C.-H., Kitaura F.-S., Prada F., Zhao C., Yepes G., 2015a, MNRAS, 446, 2621
Chuang C.-H. et al., 2015b, MNRAS, 452, 686
Cole S. et al., 2005, MNRAS, 362, 505
Coles P., Jones B., 1991, MNRAS, 248, 1
Crocce M., Scoccimarro R., Bernardeau F., 2012, MNRAS, 427, 2537
Davis M., Efstathiou G., Frenk C. S., White S. D. M., 1985, ApJ, 292, 371
de la Torre S., Peacock J. A., 2013, MNRAS, 435, 743
Drinkwater M. J. et al., 2010, MNRAS, 401, 1429
Driver S. P. et al., 2011, MNRAS, 413, 971
Eisenstein D. J., Hu W., 1998, ApJ, 496, 605
Eisenstein D. J. et al., 2005, ApJ, 633, 560
Eisenstein D. J., Seo H.-J., Sirko E., Spergel D. N., 2007, ApJ, 664, 675
Frigo M., Johnson S. G., 2005, Proc. IEEE, 93, 216
Garilli B. et al., 2014, A&A, 562, A23
Gurbatov S. N., Saichev A. I., Shandarin S. F., 1989, MNRAS, 236, 385
Hartlap J., Simon P., Schneider P., 2007, A&A, 464, 399
Hill G. J., Gebhardt K., Komatsu E., MacQueen P. J., 2004, in Allen R. E., Nanopoulos D. V., Pope C. N., eds, AIP Conf. Ser. Vol. 743, The New

Cosmology: Conference on Strings and Cosmology. Am. Inst. Phys., New York, p. 224
Howlett C., Manera M., Percival W. J., 2015a, Astron. Comput., 12, 109
Howlett C., Ross A. J., Samushia L., Percival W. J., Manera M., 2015b, MNRAS, 449, 848
Jing Y. P., 2005, ApJ, 620, 559
Kazantzidis S., Magorrian J., Moore B., 2004, ApJ, 601, 37
Kazin E. A. et al., 2014, MNRAS, 441, 3524
Kitaura F.-S., Yepes G., Prada F., 2014, MNRAS, 439, L21
Koda J. et al., 2014, MNRAS, 445, 4267
Komatsu E. et al., 2009, ApJS, 180, 330
Leclercq F., 2015, preprint (arXiv:1512.04985)
Leclercq F., Jasche J., Wandelt B., 2015, A&A, 576, L17
Lukić Z., Reed D., Habib S., Heitmann K., 2009, ApJ, 692, 217
Manera M. et al., 2013, MNRAS, 428, 1036
Marín F. A. et al., 2013, MNRAS, 432, 2654
Marín F. A., Beutler F., Blake C., Koda J., Kazin E., Schneider D. P., 2016, MNRAS, 455, 4046
Mehta K. T., Cuesta A. J., Xu X., Eisenstein D. J., Padmanabhan N., 2012, MNRAS, 427, 2168
Monaco P., Theuns T., Taffoni G., 2002, MNRAS, 331, 587
Monaco P., Sefusatti E., Borgani S., Crocce M., Fosalba P., Sheth R. K., Theuns T., 2013, MNRAS, 433, 2389
Navarro J. F., Frenk C. S., White S. D. M., 1997, ApJ, 490, 493
Padmanabhan N., Xu X., Eisenstein D. J., Scalzo R., Cuesta A. J., Mehta K. T., Kazin E., 2012, MNRAS, 427, 2132
Percival W. J. et al., 2014, MNRAS, 439, 2531
Poole G. B. et al., 2015, MNRAS, 449, 1454
Prada F., Klypin A. A., Cuesta A. J., Betancort-Rijo J. E., Primack J., 2012, MNRAS, 423, 3018
Quinn T., Katz N., Stadel J., Lake G., 1997, preprint (astro-ph/9710043)
Schlegel D. J. et al., 2009, preprint (arXiv:0904.0468)
Scoccimarro R., 2004, Phys. Rev. D, 70, 083007
Scoccimarro R., Sheth R. K., 2002, MNRAS, 329, 629
Springel V., 2005, MNRAS, 364, 1105
Taruya A., Bernardeau F., Nishimichi T., Codis S., 2012, Phys. Rev. D, 86, 103528
Tassev S., Zaldarriaga M., Eisenstein D. J., 2013, J. Cosmol. Astropart. Phys., 6, 36, (TZE)
Tonegawa M. et al., 2015, PASJ, 67, 81
White M., Tinker J. L., McBride C. K., 2014, MNRAS, 437, 2594
Zehavi I. et al., 2005, ApJ, 630, 1
Zheng Z. et al., 2005, ApJ, 633, 791
Zheng Y., Zhang P., Jing Y., Lin W., Pan J., 2013, Phys. Rev. D, 88, 103510

## APPENDIX A: IMPACT OF INITIAL CONDITION

We show the impact of our initial condition, which is given at $a = 0.5/n_{\rm step}$ for the velocity (equation 16), compared to the original one at $a = 0.1$ for both the position and velocity,

$$\boldsymbol{x}^{\rm res}(t_1) = 0, \qquad \boldsymbol{v}^{\rm res}(t_1) = 0. \tag{A1}$$

This original initial condition gives slightly better results, although our initial condition is not problematic in theory. The ansatz for COLA with $n_{\rm LPT} = -2.5$ is tuned for the original initial condition at $a = 0.1$, and the same ansatz is probably not optimal for our initial velocity at $a = 0.05$.

In Fig. A1, we plot the ratio of the matter power spectra to that of the GADGET $N$-body simulations at $z = 0.6$ for different number of steps with the original initial condition. We divide the time equally in scale factor between 0 and 1, $a(t_i) = i/n_{\rm step}$, for $n_{\rm step} = 10$, 20, 50, and 100. The original initial condition gives better accuracy around $k = 0.1\ h\,{\rm Mpc}^{-1}$, without the 2–3 per cent excess in Fig. 4; the agreement is better than 1 per cent for $k \leq 0.3\ h\,{\rm Mpc}^{-1}$. The range with accurate matter power expands as we increase the number of steps.

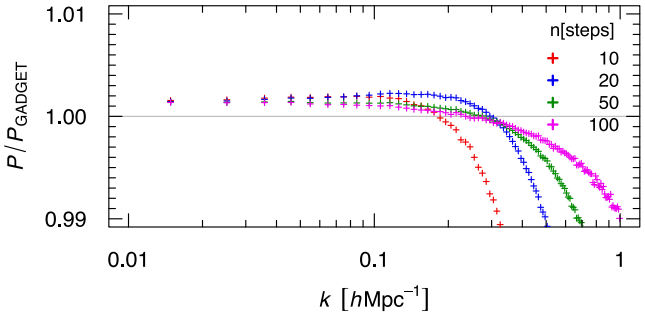


**Figure A1.** The matter power spectrum with the original initial condition, which gives slightly more accurate power spectrum than Fig. 4.

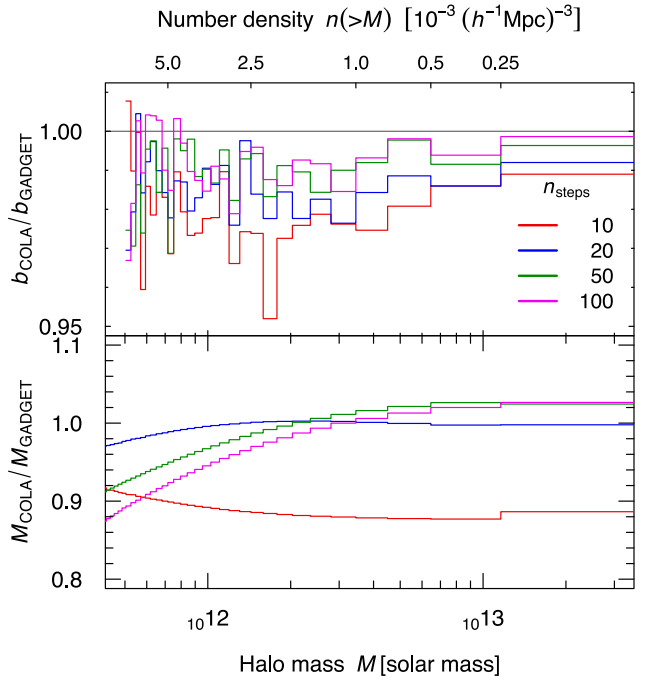


**Figure A2.** The precision of COLA halo bias (Upper panel) and halo mass (Lower panel) for various time steps. The original initial condition gives slightly better biases than Fig. 2. The accuracy become about 1 per cent for 100 steps, while the halo masses do not show monotonic convergence.

In Fig. A2, we plot the accuracy in the halo bias and mass. The original initial condition gives a slight improvement for the halo bias as well – from 5-per cent error in Fig. 2 to about 3 per cent for 10 time steps. We split the haloes to groups with an equal number density of $10^{-4}(h^{-1}\,{\rm Mpc})^{-3}$ by their mass and compute the halo bias, as we did for Fig. 2. The halo bias improves to about 1 per cent for 100 steps. The lower panel shows the mean halo mass in each group. Our COLA simulations does not converge to the GADGET simulation because we have the uniform PM grid for force computation, and that causes an additional error in the halo formation independent of time steps. The PM force recovers the correct force at a distance of about 2.7 times the PM grid size, which corresponds to a virial radius of a halo of mass $M_{200,{\rm m}} = 5 \times 10^{12}\ h^{-1}\,{\rm M}_\odot$ for our configuration; the limited force resolution below this scale explains the deviation from the correct halo mass.

In this appendix, we have shown that our excess in our matter power spectrum was caused by our initial setup for the velocity, and the accuracy of COLA simulations could improve slightly by using the original initial condition.

## APPENDIX B: THE RELATION BETWEEN THE REDSHIFT-SPACE POWER SPECTRUM AND VELOCITY POWER SPECTRUM

We derive equation (33), which shows the relation of the power spectrum in redshift space, $P^s$, and the auto- and cross- power spectra of density and the line-of-sight velocity $u \equiv v_3/(aH)$. The mass conservation between density contrast in redshift space, $\delta^s(\boldsymbol{s})$, and that in real space, $\delta(\boldsymbol{x})$,

$$[1 + \delta^s(\boldsymbol{s})]d^3s = [1 + \delta(\boldsymbol{x})]d^3x, \tag{B1}$$

for the mapping between the real-space coordinate $\boldsymbol{x}$ and the redshift-space coordinate, $\boldsymbol{s} = \boldsymbol{x} + u(\boldsymbol{x})\boldsymbol{e}_3$ (where $\boldsymbol{e}_3$ is the unit vector along the third axis), gives a formula for the density contrast in Fourier space (e.g. Scoccimarro 2004)

$$\delta_D(\boldsymbol{k}) + \delta^s_g(\boldsymbol{k}) = \int d^3x\, e^{-i\boldsymbol{k}\cdot\boldsymbol{x}} e^{-ik\mu u(\boldsymbol{x})}[1 + \delta(\boldsymbol{x})], \tag{B2}$$

where $\delta_{\rm D}$ is the Dirac delta function and $k\mu = k_3$. The relation up to the first order in $k\mu u$ is,

$$\delta^s(\boldsymbol{k}) \approx \delta(\boldsymbol{k}) - ik\mu u(\boldsymbol{k}). \tag{B3}$$

Equation (33) can be derived by taking the variance $\langle \delta^s(\boldsymbol{k})\delta^s(\boldsymbol{k})^* \rangle$,

$$P^s \approx P_{\delta\delta}(k) + 2k\mu {\rm Im} P_{\delta u} + (k\mu)^2 P_{\rm uu}. \tag{B4}$$

This is equivalent to a well-known formula by Scoccimarro (2004),

$$P^s \approx P_{\delta\delta} + 2f\mu^2 P_{\delta\theta} + f^2\mu^4 P_{\theta\theta}, \tag{B5}$$

where $\theta(\boldsymbol{x}) = \nabla \cdot v(\boldsymbol{x})/(afH)$ is the velocity divergence and $f \equiv d\ln D_1/d\ln a$ is the growth rate. It can be shown by inverting the divergence in Fourier space,

$$\boldsymbol{v}(\boldsymbol{k}) = afH\frac{i\boldsymbol{k}}{k^2}\theta(\boldsymbol{k}), \tag{B6}$$

or $u(\boldsymbol{k}) = if\mu\theta(k)/k$, assuming the vorticity is negligible, $\nabla \times v(\boldsymbol{x}) = 0$.

**Table B1.** We list the number of galaxies, $N_{\rm WiggleZ}$, the mean numbers of mock galaxies and their standard error in the mean for 3600 realisations, $\bar{N}_{\rm WiggleZ}$, and the survey volume in units of $10^7(h^{-1}\,{\rm Mpc})^3$, for the six regions in the sky decomposed to three redshift bins. The cuboid is one of the box remappings listed in Table 3. The 'overlap' is the fraction of the survey volume that overlaps in the periodic simulation box in per cent – the overlapped volume consists of two copies of the same simulation volume. Since $\Delta^{\rm Mid}$ completely overlaps with the other two redshift bins, the total, in the final row, is the sum for Near and Far redshift bins.

| Reg | $\Delta z$ | $N_{\rm WiggleZ}$ | $\bar{N}_{\rm WiZ-COLA}$ | Volume ($10^7$) | Cuboid | Overlap |
|---|---|---|---|---|---|---|
| 1 hr | Near | 6927 | 6927.63 ± 3.3 | 2.81 | $\sqrt{3}$ | 0 |
| 1 hr | Mid | 9437 | 9436.5 ± 3.4 | 4.98 | $\sqrt{3}$ | 0 |
| 1 hr | Far | 7880 | 7882.2 ± 3.1 | 7.12 | $\sqrt{3}$ | 0 |
| 3 hr | Near | 8000 | 8000.3 ± 3.6 | 2.89 | $\sqrt{3}$ | 0 |
| 3 hr | Mid | 10 241 | 10 240.7 ± 3.6 | 5.12 | $\sqrt{3}$ | 0 |
| 3 hr | Far | 8756 | 8760.0 ± 3.1 | 7.33 | $\sqrt{3}$ | 0 |
| 9 hr | Near | 15 128 | 15 131.0 ± 5.0 | 4.82 | $\sqrt{3}$ | 0 |
| 9 hr | Mid | 18 978 | 18 984.0 ± 5.1 | 8.53 | $\sqrt{3}$ | 0 |
| 9 hr | Far | 11 424 | 11 418.6 ± 3.4 | 12.20 | $\sqrt{2}$ | 0.58 |
| 11 hr | Near | 18 019 | 18 020.1 ± 5.1 | 6.25 | $\sqrt{3}$ | 0 |
| 11 hr | Mid | 22 289 | 22 299.2 ± 4.8 | 11.07 | $\sqrt{2}$ | 5.08 |
| 11 hr | Far | 13 919 | 13 894.9 ± 3.3 | 15.84 | $\sqrt{2}$ | 1.73 |
| 15 hr | Near | 22 309 | 22 312.3 ± 6.1 | 7.12 | $\sqrt{3}$ | 0 |
| 15 hr | Mid | 30 015 | 30 024.6 ± 6.1 | 12.62 | $\sqrt{2}$ | 4.88 |
| 15 hr | Far | 19 471 | 19 428.3 ± 4.4 | 18.05 | $\sqrt{2}$ | 5.66 |
| 22 hr | Near | 15 884 | 15 883.6 ± 6.5 | 3.55 | $\sqrt{3}$ | 0 |
| 22 hr | Mid | 16 146 | 16 142.7 ± 5.4 | 6.29 | $\sqrt{3}$ | 0 |
| 22 hr | Far | 11 024 | 11 025.9 ± 3.8 | 9.00 | $\sqrt{3}$ | 0 |
| Total | | 158 741 | | 97.00 | | 1.7 |

This paper has been typeset from a TEX/LATEX file prepared by the author.